Evaluation of linac-based delayed gamma neutron activation technique for copper characterization in scrap metal by means of Monte Carlo modeling

Roberto de Stefano, Aly Elayeb, Adrien Sari, Hamid Makil, Philippe Russo, Frédérick Carrel

Evaluation of linac-based delayed gamma neutron activation technique for copper characterization in scrap metal by means of Monte Carlo modeling

R. De Stefano[1*], A. Elayeb[1], A. Sari[1], H. Makil[1], P. Russo[2], F. Carrel[1]

[1] *University of Paris-Saclay, CEA, LIST, F-91129, Palaiseau, France*

[2] *ArcelorMittal, Global Research and Development, Maizières Process, F-57283, Maizières-lès-Metz Cedex, France*

[*]*corresponding author: roberto.destefano@cea.fr*

Abstract

Delayed gamma rays following neutron activation, induced by a 6 MeV linear electron accelerator (linac) coupled to a deuterium oxide photo-neutron conversion target, are simulated with MCNP6.1. The 1039 keV copper activation gamma peak is detected with a 33 % relative efficiency hyper pure germanium detector. Two copper distributions were assessed for a 2-hour irradiation followed by a 2-hour counting configuration. Homogeneously distributed copper in a planar scrap metal matrix shows ^{65}Cu detection limits of 10.01 g. A solid copper sample, modeled at five distinct positions in the planar scrap metal matrix, exhibits detection limits from 8.27 to 14.27 grams.

Keywords

Delayed gamma rays, Neutron activation analysis, linac, copper, MCNP6, detection limits

Introduction

Neutron Activation Analysis (NAA) is a legacy technique developed since the end of the ’30s [1][2]. Following its discovery, the method was used in several applied fields such as archelogy [3][4] and forensics [5]. More recently, the method is used for homeland security applications due to the growing need of threat detection in the past years [6][7]. Several NAA techniques are also widely used in the framework of foundational research subjects [8][9][10]. In regards to industrial applications NAA is still under development, for instance, for the non-destructive elemental characterization of specific manufactured pieces such as metals [11][12][13].

In the framework of its collaboration with ArcelorMittal R&D, LIST Institute from *Commissariat a l’Energie Atomique et aux energies alternatives* (CEA) is currently studying the applicability of a recent neutron activation technique that aims at estimating the amount of copper in scrap metal [14][15]. Using the 6 MeV mode, the Linatron® M9 linac from Varex Imaging Corp. housed at the SAPHIR platform of CEA Paris-Saclay is coupled to a deuterium oxide photo-neutron target. The latter is placed inside a High Density Polyethylene (HDPE) neutron interrogation cell manufactured for neutron irradiation purposes [16]. This technique presents several advantages in the scope of scrap metal characterization, due to important neutron emission intensities higher than 10^9 $n.s^{-1}$ [17], and the possibility to use the same linac along with a X-ray radiography and photon activation analysis [18][19].

This paper aims to explore the achievable performances of such a variant of NAA in the field of copper characterization in scrap metal using the SAPHIR linac at 6 MeV. In this scope, Monte Carlo simulations have been carried out with MCNP6.1 and the Activation Control Card (ACT) [20] to compute the 1039 keV delayed gamma ray from ^{65}Cu. This study focuses on a surface interrogation scenario by modeling a scrap metal planar sample with two very different copper distribution assumptions. Either copper is described with a homogeneous distribution, or with a solid disk placed at five positions in the metal matrix.

This paper reports the neutron flux behavior in the measurement cell, the 1039 keV peak contribution detected with a hyper pure germanium computed with MODAR Software (MCNP Output Data Analysis with Root) [21], and corresponding detection limits.

1. Numerical Approach

With the aim of evaluating the performance of linac-based neutron activation technique, a numerical model of the SAPHIR platform and the neutron irradiation cell formerly developed in [16] have been adapted to MCNP6.1. This version of MCNP6 was used as it implements the ACT card which allows the simulation of neutron-induced activation gamma rays for which creation and temporal behavior were validated in [22][23]. Fig. 1 illustrates the SAPHIR platform with a Linatron® M9 linac and the HDPE cell developed for neutron interrogation applications. This figure also reports a perspective representation of the main building blocks of the simulation model for the case of the solid copper disk with each element numbered from (1.) to (8.) with :

(1.) a 126.6 g copper disk-shaped sample of 3 cm radius and 0.5 cm thickness for the case of the solid copper distribution model. This element is absent for the homogeneous distribution study.

(2.) A planar shaped iron matrix of $40 \times 40 \times 0.5$ cm^3 dimensions for which 125.9 g of ^{65}Cu are added to this element for the homogeneous distribution study.

(3.) The HDPE cell with 5 cm thick walls and a $70 \times 90 \times 92$ cm^3 internal volume.

(4.) The (γ, n) deuterium oxide (D_2O) conversion target of around 16 kg described by the parallelepiped of $54.4 \times 13.6 \times 19.6$ cm^3 dimensions.

(5.) The n-type coaxial Hyper Pure Germanium (HPGe) detector crystal, defined by an air-filled cylinder of 0.7335 cm radius and 4.285 cm length placed within a germanium cylindrical body of 2.548 cm radius and 5.505 cm length.

(6.) The detector's aluminum external envelope of 3.66 cm inner radius, 6.94 inner length, and 1.5 mm thickness.

(7.) The air filling the HDPE cell cavity.

(8. a.) The Linatron® M9 tungsten collimator housing the (8. b.) primary (e^-, γ) conversion target described as pure tungsten bodies of 19.3 $g.cm^{-3}$ density.

Dimensions (in cm) related to this numerical model are reported in Fig. 2; three section representations are shown including a view from the top, and two from the sides. Each simulated component, its respective mass, volume, density and associated chemical composition for the homogeneous and the solid copper descriptions are summarized in Table 1.

The incident neutron energy distribution calculated in [17], presented in Fig. 3, corresponds to the (e^-, γ) conversion of the incident 6 MeV electron beam in tungsten followed by the (γ, n) reaction in the deuterium oxide canisters. The neutron source distribution is a 10 keV-per-bin histogram from 0 to 3 MeV, emitting an average energy and neutron emission of 0.4 MeV and 2.03×10^9 n.s^{-1} in 4π sr. The related spatial definition corresponds to a homogenous distribution in the volume of the D_2O secondary target [17]. Liquid deuterium oxide fills four separated equi-volume parallepiped-shaped adjacent canisters, justifying a single body source description.

This case scenario models the copper sample with a pure ^{65}Cu abundance. This choice comes from the fact that ^{65}Cu is the second most abundant isotope in natural copper, up to an average 30.85 % [24] and the second most likely present in scrap metal. Also, this study focuses only on the 1039 keV activation delayed gamma ray associated to radiative capture $^{65}Cu(n_{th}, \gamma)^{66}Cu$ which is one of the most intense copper activation gamma ray [25]. In more details, for this reaction resulting radioactive ^{66}Cu undergoes a β^- decay onto ^{66}Zn activation product with a 5.120(14) min half-life ; after which ^{66}Zn (produced in one of its excited states), emits the 1039 keV gamma ray of 9.23 % intensity to reach the Ground State (GS) [25].

With the aim of reaching ^{66}Zn nucleus secular equilibrium, the irradiation time period T_{irrad} has been fixed to two hours to reach a nucleus production rate higher than 99.99 %. In the same way, the 1039 keV gamma ray acquisition time $T_{acquisition}$ was fixed to two hours to count the signal of interest with a rate higher than 99.99 %. Irradiation and counting times were rounded up to two hours rather than ten times the activation product half-life to simulate more realistic acquisition times with respect to industrial applications. The associated chronogram related to this study is presented in Fig. 4.

Creation and transport of activation gamma rays such as the 1039 keV signal from copper are simulated with the ACTivation (ACT) control card from MCNP6.1 in single-step computations. For this study, only Delayed Gamma rays (DG) from non-fissionable materials are of interest, thus, parameters related to the use of the ACT card are fixed to NONFISSION=P and DG=Lines. Although the ACT card allows single-step computations, which reduces biases related to classical two-steps calculations such as reaction rate simulation and its accurate description as a secondary source [26] [27], using ACT engages an important computing power. In order to reduce computational time, activation gamma rays were evaluated with a variance reduction point photon flux F5:P tally placed in front of the HPGe detector model (see Fig. 2), and a cluster composed of around a thousand of processors, owned by CEA List Institute, has been used. Each computation was carried out using 10^{10} source-neutrons to obtain a statistical uncertainty below 4% for the 1039 keV activation gamma ray of interest.

In order to simulate the signal detected by an HPGe detector, each point photon flux F5:P output was processed with the MODAR software [21] developed by CEA IRESNE Institute. MODAR allows smearing the ideal F5:P output tally with the energy response function of a 33% relative efficiency HPGe detector following

$$S\ (E) = \int_{E'} F5{:}\,P(E') \times RF_{HPGe33\%}(E', E)dE' \quad (1)$$

Where S(E), given in counts-per-source-neutron, refers to the MODAR processed signal at energy E after smearing the MCNP F5:P output with the HPGe response function. F5:P (E') describes the point photon flux estimated at the entrance of the HPGe detector and finally the pre-calculated response function $RF_{HPGe33\%}$(E',E) defines the probability that an incident photon with energy E' leads to an energy deposit E in the 33% relative efficiency HPGe detector. $RF_{HPGe33\%}$(E',E), written in an independent ROOT® [28] macro, was formerly estimated in [21] by means of MCNP simulations where each E' energy deposit corresponds to a F8:P tally output computed in the germanium crystal volume for a given incident mono-energetic photon at energy E. Mono-energetic source photons emitted perpendicular to the front section of the crystal were defined by a disk-shaped surface of 2.725 cm radius parallel to the detectors front surface. Two thousand independent

computations allowed covering the 0 to 100 MeV energy region, for incident photon energies defined each 50 keV.

Both raw F5:P output data and MODAR processed spectrum for the computation related to Fig. 2 are presented in Fig. 5. One can notice the presence of several activation gamma rays from the main chemical components in this simulation. Activation gamma rays with intensities above 1 % in the 100 to 1800 keV energy region are reported in Table 2. Fig. 6 shows the Region of Interest (RoI) of the delayed gamma ray at 1039 keV from $^{65}Cu(n, \gamma)^{66}Cu$ reaction which is clearly visible above the active background continuum, allowing further investigations on the applicability of this method to copper characterization in scrap metal.

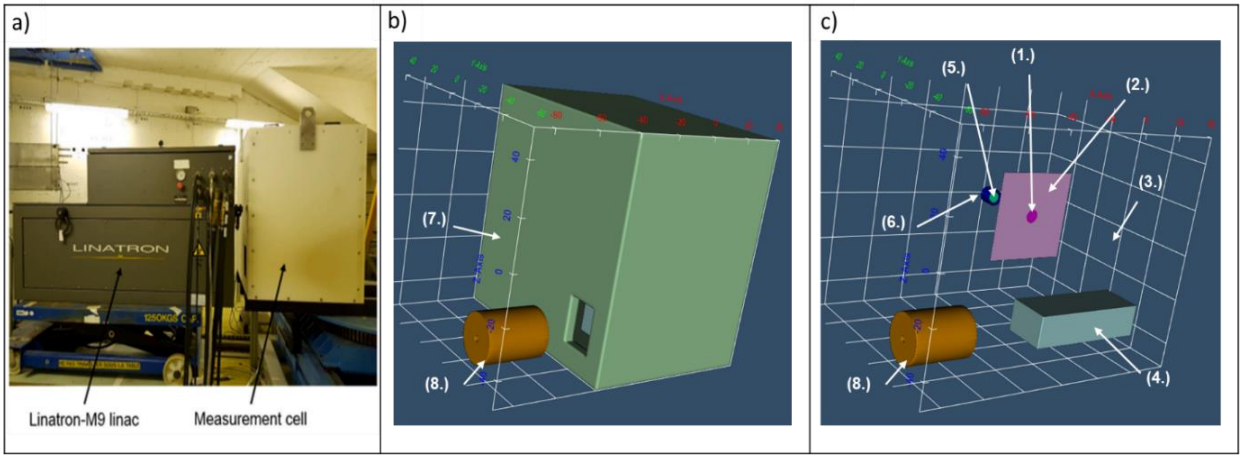

Fig. 1: a) View of the SAPHIR platform showing the Linatron® M9 linac; b) perspective representation of the MCNP6 model of the measurement cell dedicated to neutron irradiation applications; c) internal computed bodies as noted in the text.

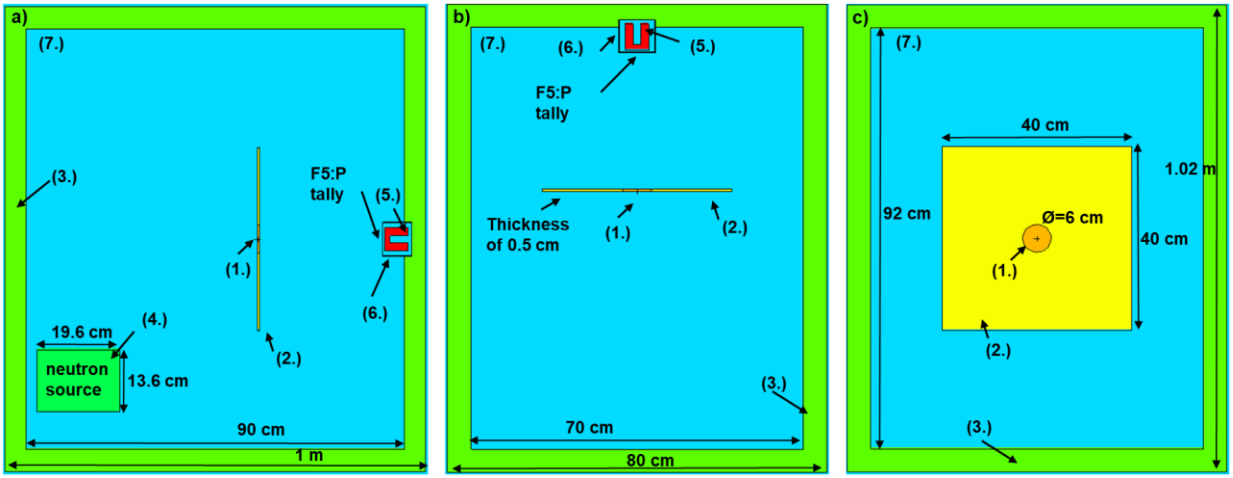

Fig. 2: Representation of the MCNP6 model (not to scale) from respectively: a) YZ view, b) XY view and c) XZ view of the neutron measurement cell. Colors are associated to the density of each model component.

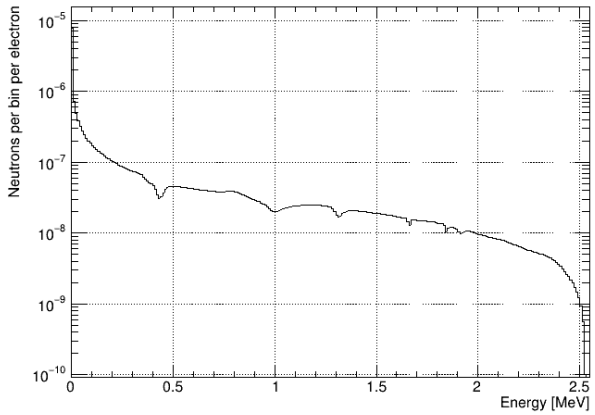

Fig. 3: Neutron energy spectrum from the 16 kg D_2O secondary target for a 6 MeV initial electron beam as simulated in [17].

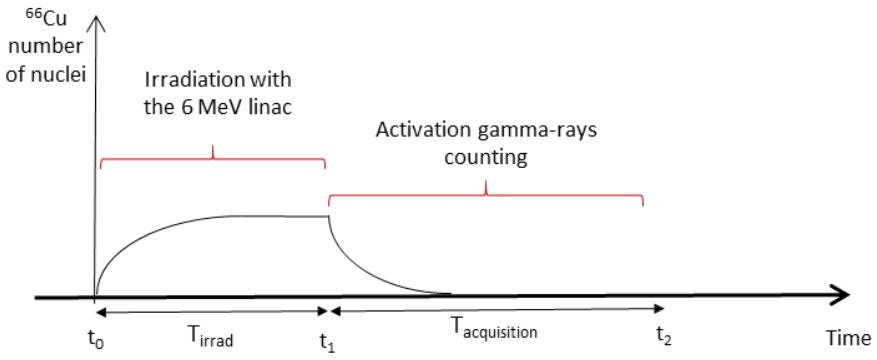

Fig. 4: Irradiation chronogram with respective time reference t_0= 0 s; t_1= T_{irrad} = $T_{acqusition}$ = 2 h; and t_2 = 4 h (not to scale).

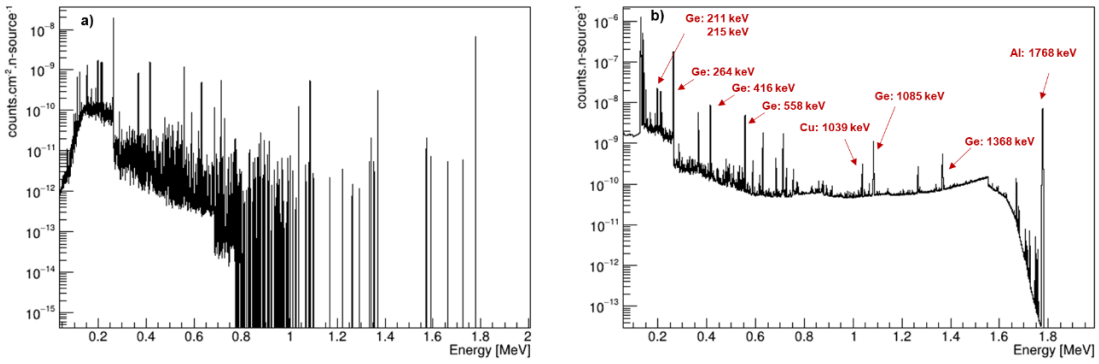

Fig. 5: a) Post-irradiation point photon flux F5:P tally spectrum and b) associated MODAR smeared signal for a pure ^{65}Cu disk placed in the middle of a scrap metal piece.

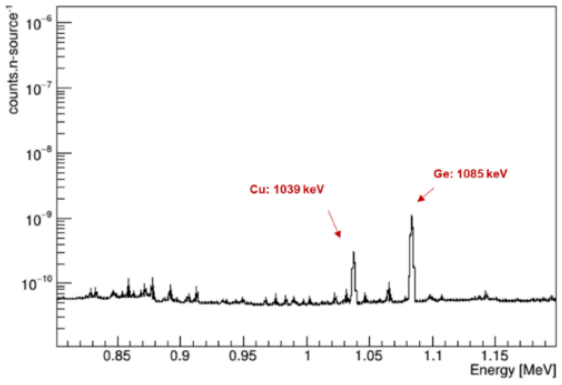

Fig. 6: Zoomed-in section in the 0.8 to 1.2 MeV region of interest for the study of the 1039 keV copper activation gamma ray.

169 Table 1: Description of the modeled components and associated chemical atomic and
170 weight fractions.

Modeled parts				**Chemical composition**			
				Solid distribution		**Homogeneous distribution**	
Body	**Volume (cm^3)**	**Mass (g)**	**Density ($g.cm^{-3}$)**	**Element**	**W. fraction**	**Element**	**W. fraction**
(1.)	14.14	126.6	8.96	^{65}Cu	1.	-	
(2.)	785.9	6.180×10^3	7.87	^{54}Fe ^{56}Fe ^{57}Fe	0.05845 0.91720 0.02435	^{54}Fe ^{56}Fe ^{57}Fe ^{65}Cu	0.05845 0.91720 0.004250 0.02010
(3.)	234.9×10^3	223.2×10^3	0.95	**Element**		**W. fraction**	
				^{1}H ^{2}H ^{12}C	0.143682 0.000033 0.856285		
(4.)	14.45×10^3	15.99×10^3	1.107	^{2}H ^{16}O	0.20118 0.79882		
(5.)	105.0	558.8	5.32	^{70}Ge ^{72}Ge ^{73}Ge ^{74}Ge ^{76}Ge	0.2120 0.2760 0.0776 0.3594 0.0750		
(6.)	27.16	73.35	2.7	^{27}Al	1.		
(7.)	1.500×10^3	1.830	1.22×10^{-3}	^{1}H ^{14}N ^{16}O	0.0011 0.7925 0.2064		
(8.a.)	8.026×10^3	154.9×10^3	19.3	^{180}W ^{182}W ^{183}W ^{184}W ^{186}W	0.0012 0.2630 0.1428 0.3070 0.2860		
(8.b.)	0.02260	0.4370					

171

172 Table 2: Main present activation gamma rays [25].

Activated Element	**Associated reaction**	**Half-life**	**Activation delayed gamma rays (keV)**	**Associated intensities (%)**
copper	$^{65}Cu(n, \gamma)^{66}Cu$	2.241 min	1039	9.23
aluminum	$^{27}Al(n, \gamma)^{28}Al$	5.120 min	1779	100
germanium	$^{76}Ge(n, \gamma)^{77}Ge$	11.30 hours	1368 784.8 558.0 264.4 1193 781.3 461.4 215.5 1085 714.4 419.8 211.0 928.9 634.4 416.3 194.8 810.4 631.8 367.4	3.30 1.32 16.1 53.9 2.57 1.01 1.27 28.6 6.05 7.17 1.23 30.8 1.05 2.08 28.8 1.77 2.27 6.95 14.0
tungsten	$^{182}W(n, \gamma)^{183m}W$	5.20 sec	160.5 107.9 102.5	5.12 18.9 2.42
	$^{184}W(n,\gamma)^{185m}W$	1.670 min	173.7 131.6	3.26 4.33
	$^{186}W(n, \gamma)^{187}W$	23.72 hours	772.9 551.5 685.7 479.5 618.3 134.2	4.12 5.08 27.3 21.8 6.28 8.80

173

174

175

176

2. Performance assessment

This section focuses on two copper distribution assumptions with the aim of evaluating the performances for both described scenarios. The first scenario corresponds to a 125.9 g homogenous distribution of ^{65}Cu throughout a plate of scrap iron metal (report to Tab. 1 for the chemical and geometrical description). The second case investigates a solid 126.6 g pure ^{65}Cu disk at various positions within an iron metal plate. The solid copper disk is described for five positions in the matrix; a $d_0 = 0$ cm centered position, and for respective distances at $d_1 = 4.23$ cm, $d_2 = 7.75$ cm, $d_3 = 14.04$ cm and $d_4 = 24.04$ cm from the center along the diagonal of the metal piece (report to Fig. 7).

All computed signals S(E) were scaled in order to obtain the number of counts for each energy bin C(E) written as

$$\boldsymbol{C}\,(\boldsymbol{E}) = \boldsymbol{S}(\boldsymbol{E}) \times \boldsymbol{E_n} \times \boldsymbol{T_{irrad}} \qquad (2)$$

Where E_n is the 2.03×10^9 n.s^{-1} neutron emission of the deuterium oxide secondary conversion target, and T_{irrad} the two hour-irradiation time. The spectra, in counts-per-bin, considering the homogeneous distribution and each position of the solid Cu disk zoomed in the 1039 keV RoI are reported Fig. 8. This figure shows a decreasing trend towards the distance *d* from the middle of the planar matrix (in fine, from the HPGe crystal) explained by a classical decrease in detection efficiencies. Indeed, the 1039 keV number of counts C(E) follow a quadratic law

$$\boldsymbol{C(E)} = \boldsymbol{-2.9223d^2 - 73.08d + 13154.4} \qquad (3)$$

For the homogenous distribution, the signal is lower than d_2 solid distribution and close to d_3. This signal behavior is explained as follows:

- (n, γ) activation rates in the plate (reported in Tab. 3) for the six studied computations are homogenous. Rates are 5340 ± 38.98 for the lowest, up to 5346 ± 5.881 act.s^{-1} for the highest.

- Detection efficiencies reported in Tab. 3 decrease with respect to the disk distance from $(2.622 \pm 0.01783) \times 10^{-4}$ for d_0 position to $(1.613 \pm 0.01274) \times 10^{-4}$ for d_4. The homogenous description result of $(2.144 \pm 0.01458) \times 10^{-4}$ is close to that for d_3 of $(2.294 \pm 0.01514) \times 10^{-4}$.

All six rates were computed with a F4:N neutron flux tally evaluated in the entire volume metal plate (i.e scrap metal and solid disk volumes for the positions study). This last was convoluted with the neutron induced (n, γ) activation reaction cross section using a FM4 tally multiplier coupled to the MT=102 parameter and SD option in order to scale this factor with the plate's and disk's volume. The results of these computations were finally scaled with the neutron emission and irradiation time. Homogenous rates for each studied configuration are explained on the one hand by the fact that iron and copper neutron activation cross-sections follow similar trends. For instance, accordingly to ENDF/B-VIII recent data libraries, ^{65}Cu and ^{56}Fe (n, γ) cross sections are 2.149 and 2.605 barns at 25.3 meV [29]. On the other hand, incident thermal neutron flux is homogenous across the XZ section at the planar metallic sample within the HDPE cavity for the homogenous and for d_0 to d_4 solid sample position in the matrix as presented in Fig. 9. To illustrate this result, thermal neutron flux cartographies where computed with a RMESH:N tally with low and high-energy thresholds of 10^{-12} and 0.025 eV fixed with the ERGSH option.

Detection efficiencies calculations were done with the 1039 keV gamma ray energy deposit for the full-energy peak, computed with a F8:P tally in the HPGe crystal volume. For the solid disk description, sources were defined as a mono-energetic 1039 keV gamma rays isotropically emitted by cylinder shaped volumes of 3 cm radius and 0.5 cm thickness placed at respective d_0, d_1, d_2, d_3, and d_4 distances from the middle of the matrix along the diagonal. For the homogeneous spread copper description, the photon source was defined as mono-energetic 1039 keV gamma rays isotropically emitted in the volume of plate shaped matrix.

This section aims at investigating the performance of linac-based neutron activation technique in terms of copper detection limits. In this scope, total counts from the 1039 keV peak have been integrated over six bins from 1036 to 1041 keV. In order to calculate the

useful net counts of the 1039 keV signal over the active background, the former were evaluated with linear extrapolations of the Compton continuum with the (a ; b) couple of parameters in the 1036 to 1041 keV region (report to Tab. 3). The standard deviation σ on the 1039 keV gamma peak over the active background continuum is calculated following a Poisson law

$$\sigma = \sqrt{N + 2 \times B_{Compton}} \quad (4)$$

Where N defines the net peak area and $B_{Compton}$ the Compton continuum active background. The associated uncertainty on the total signal (described by T) corresponds to the MCNP6 statistical uncertainty (see Tab. 3) for the 1039 keV F5:P output.

Detection Limits in counts (DL_{counts}) were calculated to cover a detection for α and β factors [30] (respectively describing a false-alarm and no-alarm probability for the signal of interest) of 2.5%

$$DL_{counts} \approx 3.92 \times \sqrt{2 \times B_{Compton}} \quad (5)$$

Uncertainty over detection limits $u(DL_{counts})$ divided by the detection limits in counts is calculated as the ratio of the uncertainty on the active background Compton continuum $u(B_{Compton})$, estimated as $\sqrt{B_{Compton}}$, over two times the Compton continuum

$$\frac{u(DL_{counts})}{DL_{counts}} = \frac{u(B_{Compton})}{2 \times B_{Compton}} \quad (6)$$

Detection limits in counts DL_{counts} were finally divided by the sensitivity coefficients S_{Cu}, resulting into the detection limits in mass DL_{mass}. S_{Cu} is calculated as the ratio of the signal net counts divided by the 125.9 g and 126.6 g homogeneous and disk-shaped copper distributions (see Tab. 3). Relative error $u(DL_{mass})$ for detection limits in grams were calculated expressed by

$$\frac{u(DL_{mass})}{DL_{mass}} = \sqrt{\left(\frac{u(DL_{counts})}{DL_{counts}}\right)^2 + \left(\frac{u(S_{Cu})}{S_{Cu}}\right)^2} \quad (7)$$

Where the uncertainty $u(S_{Cu})$ corresponds to the standard deviation σ divided the copper homogenous and disks-shaped masses. The total (T) and net counts (N) for the 1039 keV peak of interest for this study, as well as the active background Compton continuum ($B_{Compton}$) in the 1036 to 1041 keV RoI and associated detection limits, are reported in Tab. 3.

In this study, the ^{65}Cu detection limits reported in Tab. 3 increase from 8.272 ± 0.2085 g to 14.27 ± 0.5293 g for solid planar-disks positioned from d_0 to d_4 distances, in accordance with the calculated detection efficiencies trend, which decrease from d_0 to d_4. This is consistent with the notable homogeneity of activation rates for each position study. For a solid mass positioned in a planar matrix, the technique's performance is thus mainly dependent on the copper mass distance towards the detector. For the homogeneous spread copper in the metal plate, the detection limit is 10.01 ± 0.2895 g. This exhibits that the technique alone cannot discriminate homogenous copper spread on a scrap metal piece from a piece with heterogeneities on it.

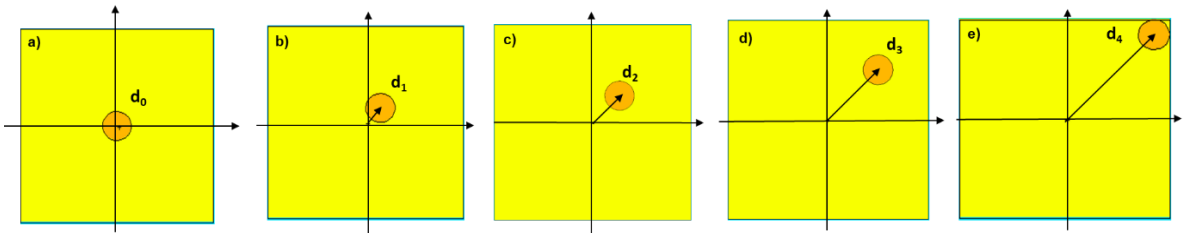

Fig. 7: XZ view from the numerical model of the metal matrix with a solid copper disk placed at a) d_0; b) d_1; c) d_2; d) d_3 and e) d_4 positions as noted in the text.

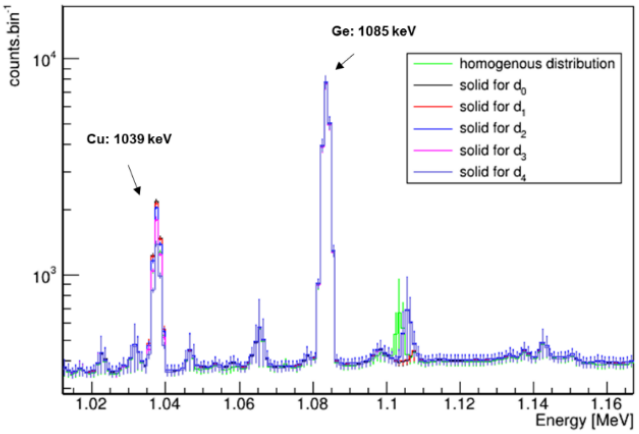

Fig. 8: 1039 keV signal obtained for a homogeneous spread *versus* solid copper mass at d_0 and at respective d_1 ; d_2, d_3 and d_4 distances from the center of the metal matrix.

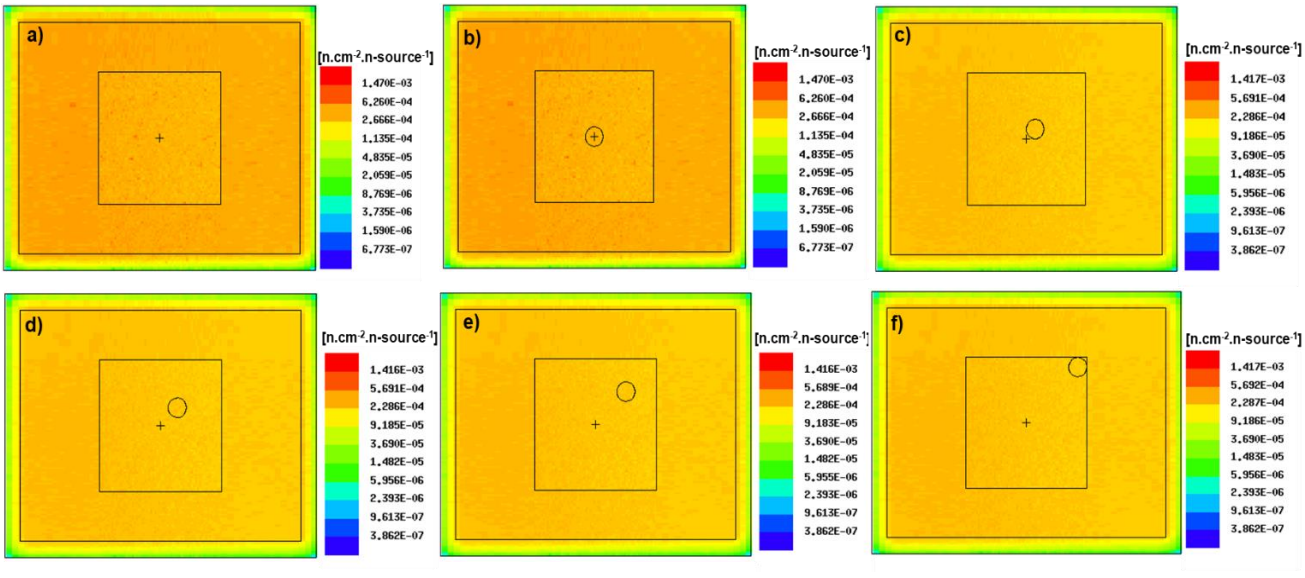

Fig. 9: Thermal neutron flux XZ representation for: a) the homogeneous copper distribution; respective solid copper mass placed at b) d_0 in the middle of the scrap metal sample; and c) d_1; d) d_2 ; e) d_3 ; f) d_4 distances from the middle of the metal piece.

282 Table 3: Detection limits considering the homogeneous distribution assumption and the
283 solid copper mass at positions d_0 to d_4.

Dist.	Homogeneous spread	Solid for d_0	Solid for d_1	Solid for d_2	Solid for d_3	Solid for d_4
Act. Rate (s^{-1})	5346 ± 0.5883	5341 ± 3.247	5341 ± 3.248	5341 ± 3.247	5341 ± 3.248	5341 ± 3.247
Det. Eff. ($\times 10^{-4}$)	2.144 ± 0.01458	2.622 ± 0.01783	2.576 ± 0.01597	2.325 ± 0.01534	2.294 ± 0.01514	1.613 ± 0.01274
F5:P Stat. Unc. (%)	1.540	2.170	2.230	2.360	2.680	3.680
T (counts)	5452 ± 83.96	6314 ± 137.0	6221 ± 138.7	5981 ± 141.2	5433 ± 145.6	4491 ± 165.3
(a;b) param.	(-2.427; 2885)	(-2.889; 3378)	(-2.849; 3339)	(-2.759; 3242)	(-2.728; 3201)	(-2.569; 3033)
$B_{Compton}$ (counts)	2189 ± 47.79	2271 ± 47.66	2284 ± 47.79	2262 ± 47.56	2206 ± 46.97	2190 ± 46.80
N (counts)	3263 ± 87.41	4043 ± 92.66	3937 ± 92.22	3719 ± 90.79	3227 ± 87.40	2301 ± 81.74
D.L. (counts)	259.4 ± 2.832	264.2 ± 2.772	264.9 ± 2.771	263.7 ± 2.772	260.4 ± 2.772	259.4 ± 2.772
S_{Cu} (g^{-1})	25.92 ± 0.6943	31.94 ± 0.7319	31.10 ± 0.7284	29.37 ± 0.7171	25.49 ± 0.6904	18.18 ± 0.6457
D. L. (g)	10.01 ± 0.2895	8.272 ± 0.2085	8.518 ± 0.2185	8.979 ± 0.2387	10.22 ± 0.2974	14.27 ± 0.5293

3. Discussion

The detection limits for ^{65}Cu of several grams are encouraging results. It proves the detectability of the signal of interest above the Compton continuum with no interference with other gamma rays. It also shows the applicability of the method for a primary rough copper mass estimation.

Additional experimental measurements of the platform's active background should be studied to justify that the 1039 keV gamma ray can be detected above the Compton continuum. Additional contributions from activation gamma rays produced in the metal matrix, modeled as a pure iron plate, but also the walls of the facility or other bodies surrounding the neutron cell, could decrease the reported performances. Also, a copper chemical description integrating ^{63}Cu present with a 69.15 % abundance in natural copper could influence these results. The high energy activation gamma ray at 1345 keV is emitted following $^{63}Cu(n,\gamma)^{64}Cu$ activation with a 12.7 hours half-life. Even though the branching ratio of this ray stands at 0.48 % [25], its contribution to the active background continuum could decrease the net signal of the 1039 keV peak. Furthermore, self-absorption and attenuation effects could alter this signal in presence of ^{63}Cu. In addition, second order effects associated to the numerical model geometrical approximations might influence the present results.

The following axis of investigation can enhance the reported performances. Detection limits can be optimized by operating the linac at 9 MeV with the same D_2O secondary target for which neutron emission was evaluated at 7.99×10^9 $n.s^{-1}$ [17]. Almost four times higher than the 2.03×10^9 $n.s^{-1}$ emission for the 6 MeV mode. A heavier mass of deuterium oxide could be used to achieve higher neutron emissions. The neutron measurement cell can be optimized by widening the irradiation cavity and using complementary graphite blocks to enhance neutron flux thermalisation similar to [31][32][33]. Additional lead bricks surrounding the outer walls of the neutron cell could limit the contribution of the active background produced outside the neutron cell, such as tungsten gamma rays reported in Tab. 2. A detector of higher relative efficiency such as the 104 % n-type coaxial HPGe used in [26][34] for similar Delayed Gamma Neutron Activation Analysis (DGNAA)

applications could be deployed. Also several HPGe detectors instead of a single detector would enhance the signal. In addition, such as 764 keV and 1114 keV inelastic scattering copper (n, n'γ) gamma rays [35] emitted during neutron irradiation can be detected. Also prompt activation gamma rays such as high-energy gamma rays at 7640 and 7910 keV [36], just after the end of each linac pulse could be detected complementarily to the 1039 keV gamma ray. In addition, the 1039 keV delayed gamma ray can be detected in inter-pulse mode rather than post-irradiation only, such as delayed gamma rays measured in [37] in the field of SNM (Special Nuclear Material) detection. For instance, the Linatron® M9 linac can be used in inter-pulse mode with 2.5 µs long pulses and a frequency ranging from 40 to 400 Hz at 6 MeV and 40 to 385 Hz at 9 MeV.

In terms of experimental applications, linac based NAA present an advantage with respect to classical techniques. For instance, the use of high-energy 14 MeV neutron sources such as a D-T generator can deteriorate the resolution of the HPGe detector [38]. This study shows that for linac based NAA, 93.5 % of the interrogating source are thermal neutrons and 6.14 % are epi-thermal. The remaining 0.36 % proportion of fast neutrons entering the HPGe range at 8.04×10^6 $n.cm^{-2}$ number-of-neutrons-per-surface-unit for the 2-h irradiation time, thus below the 10^9 $n.cm^{-2}$ threshold recommended by ORTEC constructor [39]. With the present irradiation parameters, the latter would nevertheless be reached after 124 characterizations. This estimation was computed with a F4:N tally at the entrance of the HPGe crystal volume, segmented for the respective 0 to 25.3 meV; 25.3 meV to 0.9 MeV; and 0.9 to 10 MeV regions for thermal, epithermal and fast neutrons. In the same way, the experimental application of the present method should pay a particular attention on electronics dead-time, similar to [37]. Indeed, this study shows acquisitions during and between each irradiation pulse suffer an important data loss up to 57.9 %. A particular attention should focus on the copper (n, n'γ) and prompt activation gamma rays signal reconstruction. Also, experiments with more realistic industrial scrap metal matrixes shape's and distributions should be carried as it will influence the reported performances.

In terms of complementarity with other nondestructive methods, reported signals for the homogeneous copper distribution and the five solid positions in the iron plate show the need to deploy this method with additional discrimination techniques. For instance, a

primary collimated photon activation analysis using the linac at 9 MeV and the same detector could allow the detection of a copper hot spot. Indeed, (γ, α) reaction thresholds range respectively at 6.79 and 7.61 MeV for ^{65}Cu and ^{56}Fe [40]**.** The presence of photon-induced copper activation gamma rays following ^{65}Cu(γ, α)^{61}Co reaction in the spectrum for a particular scrap metal scanned position could provide additional information of a solid copper presence in the matrix. Moreover, a primary X-ray radiography performed using the same photon source, as already studied at the SAPHIR platform in the field of nuclear waste packages characterization [18][19], could be used to complete this study. Nevertheless, in the scope of scrap metal characterization this method will be limited due to the close densities of copper (d_{Cu}=8.96 g.cm^{-3}) and scrap metal, for which the matrix is mainly composed of iron (d_{Fe}=7.87 g.cm^{-3}).

Conclusion

This study aimed to explore the potential of copper characterization in a scrap metal piece by means of linac-based delayed gamma neutron activation technique. This study focused on the use of a 6 MeV linac coupled to a 16 kg deuterium oxide secondary target emitting 2.03×10^{9} n.s^{-1} in 4π sr within a HDPE neutron measurement cell. The analysis of the 1039 keV delayed gamma ray from ^{65}Cu, and its detection with a 33 % relative efficiency HPGe was evaluated in the post-irradiation mode. Two assumptions regarding the distribution of copper in the scrap metal piece were compared: 125.9 g homogeneously spread and 126.6 g located in a disk-shaped solid mass. The solid mass was studied for five distinct positions in the matrix at increasing distances from the middle of the planar sample along the diagonal. Pure ^{65}Cu was modeled with MCNP6.1 and the signal of interest was simulated with the ACT card coupled to the MODAR software. All signals show the detectability of the 1039 keV delayed gamma ray above the active Compton Continuum background with no other activation gamma ray interferences. Mass detection limits of copper were evaluated from 8.272 ± 0.2085 g to 14.27 ± 0.5293 g for the solid disk positioned in the middle of the matrix, and positioned 33.94 cm far from the middle, following the diagonal of the plate. For the homogeneous spread copper in the metal matrix, detection limit are 10.01 ± 0.2895 g, which are encouraging performances in view

of further investigations conducted with an optimized measurement protocol. Furthermore, performances obtained with the two case scenarios and for each studied solid copper position show the interest and the technical potential of the linac-based neutron activation technique with respect to classical NAA.

Acknowledgment

Particular acknowledgement to Dr. Cédric Carasco from CEA IRESNE for his feedback and advice regarding MODAR Software source codes.

References

[1] G. Meyer, “L’analyse par activation de neutrons de réacteur”, J. Phys. IV France 103 (2003), DOI: 10.1051/jp4:20030009.

[2] V.P Guinn, C.D Wagner, "Instrumental Neutron Activation Analysis", *Anal. Chem.*, 32, 3, pp. 317–323, 1960.

[3] M.D Glascok, H. Neff, “Neutron activation analysis and provenance research in archeology”, *Meas. Sci. Technol.* vol. 14, n°9, July 2003.

[4] R. J. Speakman, M.D Glascok, “Acknowledging fifty years of neutron activation analysis in archeology”, *Archeometry*, vol. 49, Iss. 2, pp.179-183, May 2007.

[5] R. F. Coleman, “The application of neutron activation analysis to forensic science”, *Journal of Forensic Science Soc.*, 6: 19-22, Jan. 1967.

[6] M. Gierlik et al., "SWAN - Detection of explosives by means of fast neutron activation analysis" *Nucl. Instrum. Methods Phys. A*, vol. 834, pp.16-23, 2016.

[7] C. Carasco, B. Pérot, A. Sardet, "Measuring hydrogen with fast neutrons : Application to organic materials identification in cargo containers" *Nucl. Instrum. Methods Phys.* A, vol. 951, 163030, 2020.

[8] J. H. Crocket, “Neutron activation analysis for noble metals in geochemistry”, *Activation Analysis in Geochemistry and Cosmochemistry*, pp. 339-351, 1971.

[9] W. Kiesl, “Determination of traces element sin meteoritic phases by Neutron activation analysis”, *Activation Analysis in Geochemistry and Cosmochemistry*, pp. 243-251, 1971.

[10] V. Cercasov, “Investigation of atmospheric particulates deposited on leaves using instrumental neutron activation analysis", *Activation Analysis in Geochemistry and Cosmochemistry*, pp. 293-297, 1971.

[11] I. Popescu et al., "Multielemental analysis of metallurgical samples by thermal neutron activations", *Journal of Radioanalytical and Nuclear Chemistry*, Vol. 213, pp. 369-376, 1996.

[12] I. Kuleff, E. Pernicka, “Instrumental neutron activation analysis of native copper: Some methodological considerations", *Journal of Radioanalytical and Nuclear Chemistry*, vol. 191, pp. 145-161, 1995.

[13] J. Hampel, “Fast determination of impurities in metallurgical grade silicon for photovoltaics by intrumental neutron activation analysis”, *Applied Radiation and Isotopes*, vol. 69, Iss. 10, pp. 1365-1368, 2011.

[14] A. Sari, S. Garti, F. Lainé, H. Makil, N. Dufour, R. Woo, F. Carrel, P. Russo, “Detection and quantification of copper in scrap metal by linac-based neutron activation analysis”, *Applied Radiation and Isotopes*, 2020, vol. 166, 109339.

[15] R. De Stefano, A. Sari, H. Makil, F. Carrel, P. Russo, “Simulation of photo-neutron induced activation delayed gamma rays for copper characterization in scrap metal”, IEEE Nuclear Science Symposium and Medical Imaging Conference, 28th International Symposium on Room-Temperature Semiconductor Detectors, 16-23 Oct. 2021.

[16] A. Sari, F. Carrel, F. Lainé, A. Lyoussi, “Design of a Neutron Interrogation Cell Based on an Electron Accelerator and Performance Assessment on 220 Liter Nuclear Waste Mock-Up Drums”, IEEE Transactions on Nuclear Science, Institute of Electrical and Electronics Engineers, 2014, 61 (4), pp. 2144 – 2148, 10.1109/TNS.2013.2288240.

[17] A. Sari, F. Carrel, F. Lainé, “Characterization and optimization of the photo-neutron flux emitted by a 6 or 9 MeV electron accelerator for neutron interrogation measurements”. IEEE, TNS, Vol. 65, Issue 9, Sept. 2018.

[18] F. Carrel, M. Agelou, M. Gmar et al., “Coupling high energy radiography and photon activation analysis (PAA) to optimize the characterization of nuclear waste packages”, AIP conference proceedings, 1194, 3 (2009)

[19] F. Carrel et al., “Characterization of old nuclear waste packages coupling photon activation analysis and complementary non-destructive techniques”, IEEE, TNS, Vol. 61, Iss. 4, pp. 2137-2143, April 2014.

[20] J. W. Durkee (2012), “MCNP6 delayed-particle verification and validation”, Rev. 5, LA-UR-12-00676.

[21] C. Carasco, “MCNP output data analysis with ROOT, (MODAR)”, *Comput. Phys. Commun.*, Vol. 181, pp. 2210–2211, 2010.

[22] R. De Stefano, B. Perot, C. Carasco, E. Simon, "Simulation of delayed gamma rays from neutron induced fissions using MCNP 6.1", 6th International Conference on Advancements in Nuclear Instrumentation Measurement Methods and their Applications, 17– 21 June 2019.

[23] E. Simon et al. "Feasibility study of fissile mass quantification by photofission delayed gamma rays in radioactive waste packages using MCNPX", *Nucl. Instrum. Methods Phys. A*, Vol. 840, pp. 28–35, 2016.

[24] P.G Georgopoulos et al., "Environmental copper : its dynamics and human exposure issues", Journal of Toxilocology and Environmental Health, Part B, Vol. 4, pp. 341-394, 2001.

[25] NUCLEIDE-LARA on the web (2018), *[Available Online]*, http://www.nucle ide.org/Laraw eb/index .php

[26] T. Nicol et al., "Feasibility study of 235U and 239Pu characterization in radioactive waste drums using neutron-induced fission delayed gamma rays", *Nucl. Instrum. Methods Phys. A*, Vol. 832, pp. 85–94, 2016.

[27] T. Nicol et al., "Quantitative comparison between PGNAA measurements and MCNPX simulations", *Journal of Radioanalytical and Nuclear* Chemistry, Vol. 308, pp. 671–677, 2016.

[28] Brun R., Rademakers F., ROOT: An object-oriented data analysis framework, Nucl. Instrum. Methods Phys. Res. A, 389 (1997), pp.81-86.

[29] Brown D.A, et al. "ENDF/B-VIII.0: The 8th major release of the nuclear reaction data library with CIELO-projections cross sections, new standards and thermal scattering data", Nucl. Data Sheets, 148 (2018), pp.1-142

[30] *« Détermination du seuil et de la limite de détection en spectrométrie gamma », https://inis.iaea.org/collection/NCLCollectionStore/_Public/21/054/21054264.pdf, Cea Report n°CEA-R-5506, pp.40, 1989 [Available Online]*

[31] K. A. Jordan, T. Gozani, and J. Vujic, "Differential die-away analysis system response modeling and detector design", Nucl. Instrum. Methods Phys. Res. Sect. Accel. Spectrometers Detect. Assoc. Equip., vol. 589, no. 3, pp. 436–444, May 2008.

[32] F. Jallu, C. Passard, and E. Brackx, "Application of active and passive neutron non destructive assay methods to concrete radioactive waste drums", *Nucl. Instrum. Methods Phys. Res. Sect. B Beam Interact. Mater. At.*, vol. 269, no. 18, pp. 1956–1962, Sep. 2011.

[33] R. Antoni, C. Passard, B. Perot, F. Guillaumin, C. Mazy, M. Batifol, G. Grassi, "Reduction of the uncertainty due to fissile clusters in radioactive waste

characterization with the Differential Die-away Technique", *Nuclear Inst. and Methods in Physics Research. A,* Vol. 895, pp. 144–149, 2018.

[34] T. Nicol et al., "HPGe-detector shielding optimization with MCNP for the MEDINA neutron activation cell", *Journal of Radioanalytical and Nuclear Chemistry*, Vol. n° 310, pp. 865-874, 2016.

[35] B. Holmqvist, T. Wiedling, "Inelastic Neutron Scattering Cross Sections of ^{63}Cu and ^{65}Cu in the Energy Region 0.7 to 1.4 MeV", Aktiebolaget Atomenergy Report n°AE-150, 1964

[36] J. Charbucinski, J. Malos, A. Rojc, C. Smith, "Prompt gamma neutron activation analysis method and instrumentation for copper grade estimation in large diameter blast holes", *Applied Radiation and Isotopes*, Vol. 59, Iss. 2-3, pp. 17-203, 2003

[37] R. De Stefano, B. Pérot, C. Carasco et al., "Pulsed neutron interrogation with PVT plastic scintillators to detect nuclear materials", *Nuclear Inst. And Methods in Physics Research. Sect. A*, Vol. 976, 164276, 2020.

[38] G. Gilmore, "Practical gamma ray spectrometry", *DOI:10.1002/9780470861981,* (2008)

[39] AMETEK-ORTEC, "Detecting High Energy Gamma Rays from Neutron Interactions: Neutron Damage and HPGe Detectors", https://www.ortec-online.com, *[Available Online]*

[40] IAEA B. "Handbook on photonuclear data for applications – Cross-sections and spectra, TECDOC-1178" (2000)